

Photo Rechargeable Li-Ion Batteries using Nanorod Heterostructure

Electrodes

Amar Kumar^a, Pallavi Thakur^a, Rahul Sharma^a, Anand Puthirath^b, Pulickel M. Ajayan^b, and

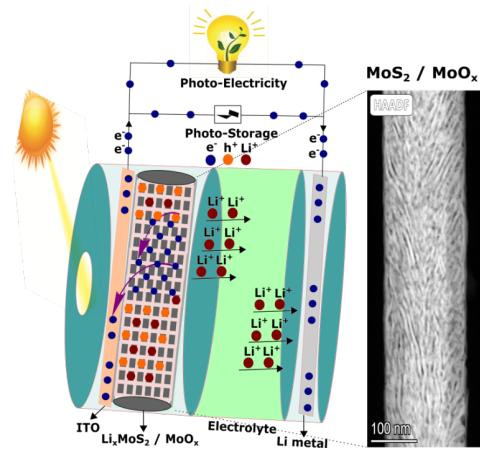
Tharangattu N. Narayanan^{a*}

^a Tata Institute of Fundamental Research - Hyderabad, Hyderabad, Telangana 500046, India

^b Department of Materials Science and Nano-engineering, Rice University, Houston, Texas
77005, United States

(Email*: tnn@tifrh.res.in)

ToC



The working (photo-charging) of single nanorod containing $\text{MoS}_2/\text{MoO}_x$ heterostructure based two-electrode solar battery. A high-resolution high angle annular dark-field image of the nanorod is also shown indicating the structure containing both amorphous and crystalline regions.

Abstract: New ways of directly using solar energy to charge electrochemical energy storage devices such as batteries would lead to exciting developments in energy technologies. Here, a two-electrode photo-rechargeable Li-ion battery is demonstrated using nanorod of type II semiconductor heterostructures with in-plane domains of crystalline MoS₂ and amorphous MoO_x. The staggered energy band alignment of MoS₂ and MoO_x limits the electron holes recombination and cause holes to be retained in the Li intercalated MoS₂ electrode. The holes generated in the MoS₂ pushes the intercalated Li⁺ ions and hence, charge the cell. Low band gap, high efficiency photo-conversion and efficient electron-hole separation help the battery to fully charge within a few hours with a low power light. The proposed concept and materials could enable next generation stable solar chargeable battery electrodes, in contrast to the reported materials.

Keywords: Solar battery; Li-ion battery; Type II Semiconductor Heterostructure; MoS₂; MoO_x.

Introduction:

A fully photo rechargeable Li-ion batteries would revolutionize today's energy conversion/storage paradigm. Two electrode solar cells are typically used to store solar energy where solar energy is first converted to electricity which is, then, stored in a conventional two electrode battery.¹ The inherent limitation of this process is the weight caused by a solar cell stack since a maximum voltage which can be delivered by a single junction solar cell is ~0.6-1.0 V only, which is insufficient for electrochemical storage systems such as Li-ion batteries.² Further, this whole process involves two conversion steps: conversion of solar energy to electricity by solar cell and the electricity conversion as electrochemical energy in a battery. Two separate systems having four electrodes cause large conversion loss and also increase the overall intricacy, weight, and cost.³ Highly efficient, low-cost, compact, and light-weight solar energy storage systems are of high demand in sectors of different kinds, such as in high energy density demand portable devices, solar vehicles, solar impulse planes, satellites, etc.^{4,5,6}

This concept was initially proposed by Hodes *et. al.* in 1976, where they have shown a three-electrode system comprised of cadmium selenide, sulfur, and silver sulphide (CdSe/S/Ag₂S).⁷ In this system, one of the components was acted as photo-electrode while others as the components for the energy storage. Such effortshave continued with other three-electrode systems, such as n-cadmium selenide telluride/cesiumsulfide/tin sulfide⁸ and hybrid Titania (TiO₂) poly(3,4-ethylenedioxythiophene) as photo anode and a perchlorate (ClO₄⁻)-doped polypyrrole counter electrode.

This approach was improved by using a two-electrode system with a hybrid mixture of lithium iron phosphate (LFP) nanocrystals and N719 dye as the active photo-electrode assembled

with lithium metal as counter electrode.⁹ The N719 dye acts as photon absorber and LFP as cathode. In this system, during the photo-charging, the electrons produced during the photo-excitation of the dye generate holes in the valance band which repel Li^+ ions from their intercalated state. The continuous photo-conversion drives the battery to reach back in the charged state (in 30 hours (hr) with 200 W solar spectrum (simulator)).⁹ But the LFP-N719 hybrid system provided a photo-conversion efficiency of $\sim 0.06\%$ only.⁹ Further it was observed that soon after the first cycle, the charge capacity started fading due to dissolution of the organic dye in to the organic electrolyte.

A different approach was attempted where a polycrystalline metal halide based 2D perovskite was used as a photo-active electrode ($(\text{C}_6\text{H}_9\text{C}_2\text{H}_4\text{NH}_3)_2\text{PbI}_4$) that could provide both the energy storage (battery functionality) and the photo charging (photovoltaic functionality) together.¹⁰ This perovskite system provided a low photo conversion efficiency of $\sim 0.034\%$. Further, the system suffered from various other challenges such as the conversion reaction between lithium and perovskite generating lead (Pb) where it can further make alloy with lithium causing large volume expansion.

More recently it was reported that organic molecule based photo-electrode could be used for photo-charging.¹¹ Absorption of light of a desired wavelength by lithiated tetrakislawsonone electrodes generates electron-hole pairs. The holes oxidize the lithiated tetrakislawsonone to tetrakislawsonone while the generated electrons flow from the tetrakislawsonone cathode to the Li metal anode through outer circuit. Authors showed $\sim 12\%$ increase in discharge capacity due to competitive charging in the presence of light. Yet the dissolution of organic molecule in organic

solvents used in the electrolytes limits its long-term performance. Further, tetrakislawsonone absorbs only violet light which is a minor component of the entire solar spectrum.

Semiconductors possess well defined band gaps and they can be tuned to make heterostructures with other semiconductors having different band gaps resulting in the separation of photo-excited electron-hole pairs.^{12,13} Further, some of these semiconductors have layered structure where they can be employed as active cathode or anode materials for different metal ion battery systems such as Li^+ , Na^+ , K^+ , etc. Such semiconductors include oxides and sulphides such as TiS_2 , MoO_3 , MoS_2 , TiO_2 etc.^{14,15,16,17,18,19} They have been shown to exhibit high stable energy capacity (300-1000 mAh g^{-1}) for many cycles of operation when used in conventional metal-ion battery systems. By virtue of their two-dimensional (2D) structure in isolated form, they can also be used for thin- batteries. Further, heterostructures of these 2D materials show high energy capacity as compared to conventional 2D material.²⁰

Photo-excited electron-hole separation is a bottleneck in any semiconductor as the high exciton binding energy and fast recombination can inhibit the photo-recharging process. A type-II semiconductor heterostructure (having staggered band alignment) of two different semiconductors can effectively separate the generated electron-hole pairs.²¹ In this case, after the excitation, all the electrons get accumulated in the low energy conduction band of one semiconductor while the holes get transferred to the high energy valence band of the second semiconductor.²¹ Further, nanostructured light absorbers have advantages such as shortening of carrier collection pathways along with improved light distribution.²² Such an architecture provides large the surface area for Li^+ ion diffusion and control over the volume expansion during cycling.²³

Here, we propose such a novel heterostructure of MoS₂/MoO_x nanorod (NR) as a single nanostructured electrode for two electrode photo-rechargeable Li-ion battery. The crystalline MoS₂ acts as Li⁺ intercalating electrode where on photoexcitation holes remain in the matrix while the electrons get transferred to MoO₃ and then to the current collector *via* the conductive carbon matrix. The mechanism of charge separation is initially proven using photocurrent measurements followed by the demonstration of a photo-rechargeable cell of Li⁺, where photo-charging and extending the discharge time using light are demonstrated. A high surface area photo-active Li⁺ intercalable electrode is developed. MoO₃ nanorods are initially synthesized by a hydrothermal method, reported elsewhere²⁴ followed by their partial surface sulfurization by a chemical vapour transport deposition (CVD) method to grow nanostructured MoS₂ regions (detailed in method section-1). In a partially sulfurized MoO₃ i.e. MoS₂/MoO_x (MoO_x nomenclature is established later) nanorods, both MoS₂ and MoO₃ are exposed at the surface. MoS₂ has higher exposed surface area compared to that of MoO_x, which is confirmed by scanning transmission electron microscopy (STEM) and high angle annular dark field (HAADF) analyses, discussed in the later part. Covalently attached MoS₂ with MoO_x domains in MoS₂/MoO_x structure can offer high light-matter interaction and high intercalation area for Li⁺, and hence without causing the mass transfer limitations in the electrochemical lithiation/delithiation processes.

Results and discussion:

(a) *Structure and Chemical Nature of MoS₂/MoO_x NRs:*

The morphology of the photo-active electrode plays an important role in attaining the high photo-conversion efficiency. Maximal surface area of the heterostructure should be exposed to the light, and electrons should be easily transferrable to the outer circuit after they get accumulated in the low energy conduction band of the heterostructure. As mentioned before, orthorhombic α -MoO₃ nanorods (NR) were synthesized *via* a hydrothermal process (figure 1(a)).²⁴ A partial sulfurization of MoO₃ surface by a CVD technique (details in method section-1 SI) is then conducted. For comparison, the MoO₃ NRs were completely sulfurized and converted to MoS₂ NRs as well, by the same procedure employing longer growth time (figure 1 (a)).

The structure and morphology of all the three samples MoO₃ NR, MoS₂ NR, and the MoS₂/MoO_x NR were confirmed by scanning electron microscopy (SEM) imaging (figure S1). All the samples possess porous nanorod morphology with an average size of \sim 200 nm diameter and 1-2 μ m length. Furthermore, the energy dispersive spectroscopy (EDS) based elemental mapping shows the uniform distribution of molybdenum and oxygen in MoO₃ NR, molybdenum and sulphur in MoS₂ NR whereas molybdenum, oxygen, and sulphur in MoS₂/MoO_x NR (figure S1), indicating the formation of the chemical structure as assigned.

To further confirm the chemical structure of NRs, Raman spectroscopy analysis was carried out. Raman spectrum of the MoO₃ NR (figure 1 (b), blue curve) shows the following vibrational modes: at 156 cm⁻¹ (A_g, B_{1g}) originating from the translation of the rigid chains, at 290 cm⁻¹ (B_{2g}, B_{3g}) a doublet comprised of wagging modes of the terminal oxygen atoms, at

666.5 cm^{-1} (B_{2g} , B_{3g}) corresponds to the asymmetric stretching of the Mo–O–Mo bridge along the c axis, at 820 cm^{-1} (A_g , B_{1g}) is a symmetric stretch of the terminal oxygen atoms, and at 995 cm^{-1} (A_g , B_{1g}) is the asymmetric stretch of the terminal oxygen atoms.²⁵ This confirms the formation of MoO_3 . The Raman spectrum of MoS_2 NR shows vibrational modes correspond to that of E_{2g} (379 cm^{-1}) and A_{1g} (405 cm^{-1}), figure 1 (b), black curve. This shows the typical behaviour of bulk 2H- MoS_2 .²⁶ Hence, it confirms the conversion of MoO_3 to MoS_2 nanorods with bulk characteristics. Subsequently, characteristics modes of vibration for both the components i.e. MoO_3 and MoS_2 , were observed in partially sulfurized MoO_3 nanorods ($\text{MoS}_2/\text{MoO}_x$ NR, figure 1 (b), red curve). However, the Raman shifts corresponding to E_{2g} (380 cm^{-1}) and A_{1g} (403 cm^{-1}) modes of vibration in $\text{MoS}_2/\text{MoO}_x$ NR are red shifted by ~ 2 cm^{-1} in comparison to that in MoS_2 NRs (figure S2 (a)). This indicates the presence of a few layered MoS_2 on MoO_3 nanorods.²⁷ Furthermore, broadening in the MoO_3 Raman modes in $\text{MoS}_2/\text{MoO}_x$ NR shows the possibilities of oxygen vacancies generated in MoO_3 forming MoO_x (Figure S2 (b)).²⁸

Furthermore, X-Ray Photoelectron spectroscopy (XPS) analysis was performed to study the oxidation states of the atoms in each NRs. The XPS survey spectra (figure 1 (c)) of the samples confirm the presence of Mo (3d) and O (1s) in MoO_3 NR, Mo (3d) and S (2p) in MoS_2 NR while all the three elements, Mo (3d), O (1s), and S (2p), in $\text{MoS}_2/\text{MoO}_x$ NR.

The high resolution XPS spectra of each of the elements were collected from all the samples. For MoO_3 NR, Mo 3d shows two peaks positioned at 231.3 eV and 234.4 eV (Figure S3 (a)), arising due to spin-orbit splitting of Mo 3d_{5/2} and Mo 3d_{3/2}, respectively. This indicates the presence of Mo^{6+} chemical state. The binding energy (BE) peak at 529.10 eV (Figure S3 (d))

is ascribed to O 1s of MoO₃. This corroborates the formation of molybdenum trioxide (MoO₃) nanorods.

In MoS₂ NR, four distinct peaks (Figure S3 (c)) are observed for Mo 3d, they correspond to that of Mo⁴⁺ and Mo⁵⁺ chemical states. Two peaks at the BEs of 228.0 eV and 231.0 eV correspond to Mo⁴⁺ while the other two at the BEs of 229.2 eV and 232.0 eV correspond to Mo⁵⁺ chemical state (all the peaks are normalised by C 1s peak).²⁹ The peak at 225.5 eV relates to the S 2s of MoS₂. In addition to this, S 2p peak (Figure S3 (f)) is fitted with three peaks that correspond to S2p_{3/2} at 160.7 eV, S2p_{1/2} at 162.0 eV, and edge S at 163.3 eV.³⁰

The high resolution XPS spectra of Mo 3d for MoS₂/MoO_x NR (Figure S3 (b)) also show four peaks. Here, the two peaks positioned at the BEs of 229.1 eV and 232.2 eV are indicating the presence of Mo⁵⁺ chemical state as in MoS₂,³¹ while the other two low intensity broad peaks at the BEs of 230.6 eV and 234.0 eV indicate the presence of Mo⁶⁺ chemical state. A small shift in BE for Mo⁶⁺ 3d_{5/2} is due to signals from lower oxidation (Mo⁵⁺) state which are tailing in lower binding energy.²⁹

The O 1s in MoS₂/MoO_x NR (Figure S3 (e)) shows two peaks at the BEs of 529.9 eV and 531.2 eV, indicating the presence of metal oxide O 1s and sub-oxide, respectively. Hence, the heterostructure has mixture of molybdenum oxides and suboxides (MoO_x). These suboxides impart better conductivity and improve the charge transfer.¹² The signals at the BEs 226.3 eV, 161.9 eV, and 163.1 eV are corresponding to S 2s, S 2p_{3/2}, and S 2p_{1/2}, respectively (Figure S3 (g)).

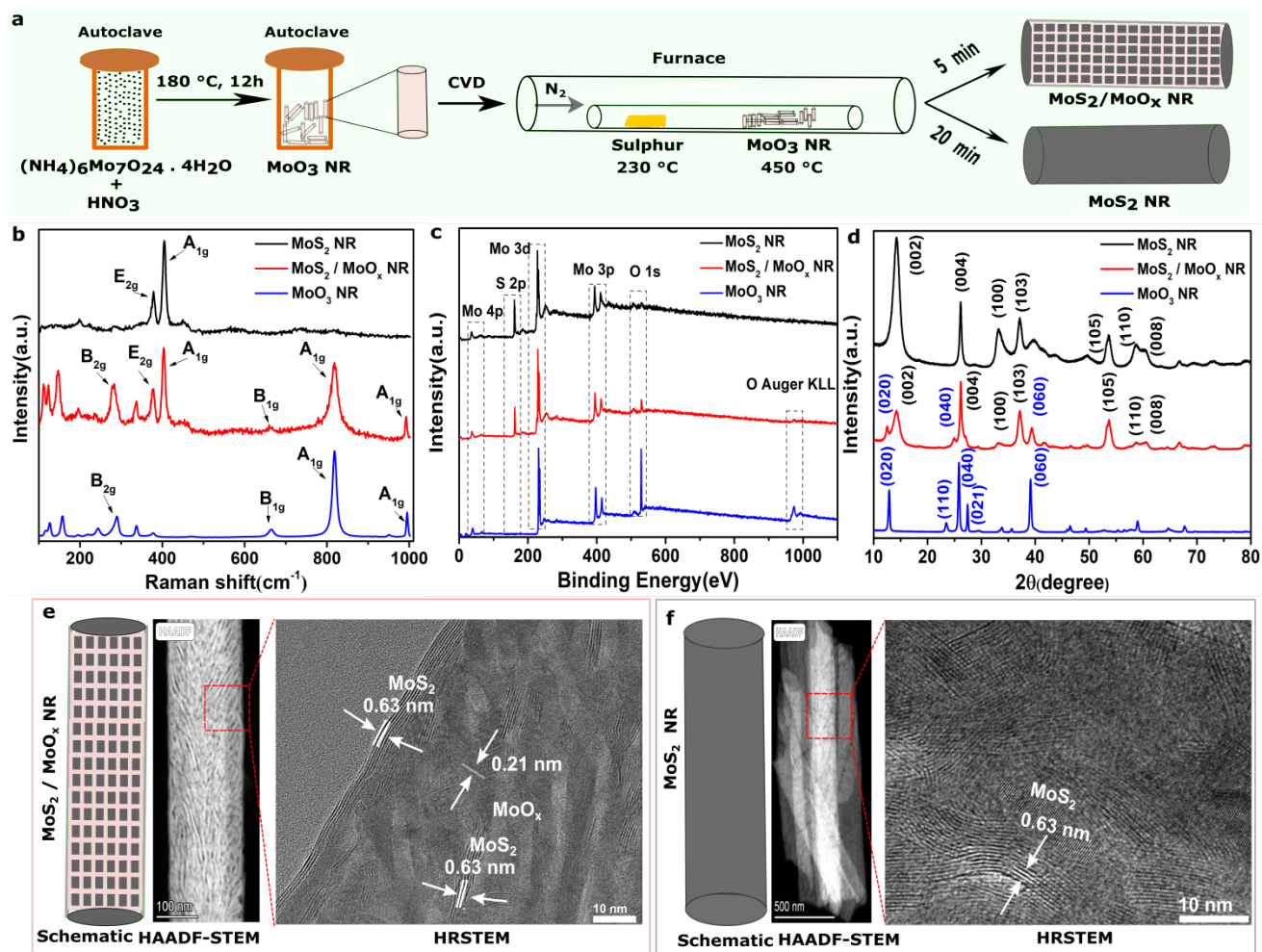


Figure 1. (a) Schematic of the reaction procedure for the synthesis of MoO₃ NRs, hetero-structured MoS₂/MoO_x NRs, and MoS₂ NRs. The characterisations of MoO₃ NR, MoS₂/MoO_x NR, and MoS₂ NR using (b) Raman analysis, (c) XPS survey scan, and (d) XRD, indicating their characteristic features as explained. STEM and HAADF images of, (e) MoS₂/MoO_xNR and (f) MoS₂ NR along with their schematics of the structures.

The crystalline structure of all the samples was studied using by powder X-ray diffraction (XRD) technique (Figure 1 (d)). Diffraction peaks for MoO₃ NR (blue) indicates that of the pure α -MoO₃ crystalline phase.³² The diffraction peaks of MoS₂ NR (black) can be indexed as (002), (004), (100), (103), (105), (110), and (008) planes of hexagonal MoS₂ crystal.³³ However, the

diffraction peaks corresponding to only (0k0) planes of MoO_3 are found in $\text{MoS}_2 / \text{MoO}_x$ hybrid structure. Some of the crystalline planes of $\alpha\text{-MoO}_3$ have converted to amorphous $\alpha\text{-MoO}_3$ during the sulfurization process. This conversion is already confirmed by XPS analysis of $\text{MoS}_2 / \text{MoO}_x$ NR.

STEM analysis was also carried out on all the three samples. In the STEM-HAADF image, various bright and dark phases were observed on the surface of $\text{MoS}_2/\text{MoO}_x\text{NR}$ (figure 1 (e)) (additional information in figure S4). The bright phase corresponds to that of MoS_2 as it is more crystalline compared to the MoO_x in corroboration with the XRD analysis. The HRSTEM images show the inter planar distance of 0.63 nm, belongs to the crystalline MoS_2 .³⁴ While the MoO_3 has converted to mix-oxides (MoO_x). An interplanar spacing of 0.21nm (corresponds to (002)) is observed for MoO_x which is slightly higher than the reported oxygen vacancies containing MoO_x .³⁵ Thus, in $\text{MoS}_2/\text{MoO}_x$ NRs, a few layered crystalline MoS_2 sheets are distributed over the molybdenum mix-oxides (MoO_x) nanorods.

(b) UV Absorption and Photocurrent Measurements:

In order to efficiently separate the photoinduced carriers, a rational design of semiconductor heterostructure is highly needed. It includes narrowing the band gap and better separation of electron hole pair. In this study, the staggered band position of $\text{MoS}_2/\text{MoO}_x$ system facilitates a better electron-hole separation on the absorption of light (figure 2 (a) and further details of band alignment in supporting information, section-3).

The absorption spectra of all the three samples were studied using UV-Vis spectroscopy technique. The powder samples were dispersed in ethanol for the absorption measurements.

MoO₃ NR shows absorption edge at 438 nm and absorption maximum at 300 nm³⁶ while MoS₂ NR shows absorptions at 647 nm and 707 nm (figure 2 (b)).³⁷ However, in MoS₂/MoO_x NR, the absorption maximum is blue-shifted as compared to the bulk MoS₂ due to the presence of only a few layers of MoS₂ present over MoO_x (figure 2 (b), red curve).³⁷ An additional absorption maximum at 496 nm is also observed due to oxygen vacancies in MoO_x.³⁵ This further confirms the oxygen vacancies produced in MoO_x.

In order to charge a photo-rechargeable battery, a large number of photo-electron generation is utmost important. Therefore, photo-response of the active material (MoS₂/MoO_x NR) was tested in 0.1 M Na₂SO₄ solution after coated on a glassy carbon electrode with an applied bias voltage of 0.3 V vs Ag/AgCl reference electrode. The photo-response was tested with a green light source (using an LED of 533 nm and 50 mW) and a red light source (an LED of 633 nm, 50 mW), as the white light contains maximum of these wavelengths' contribution.³⁸

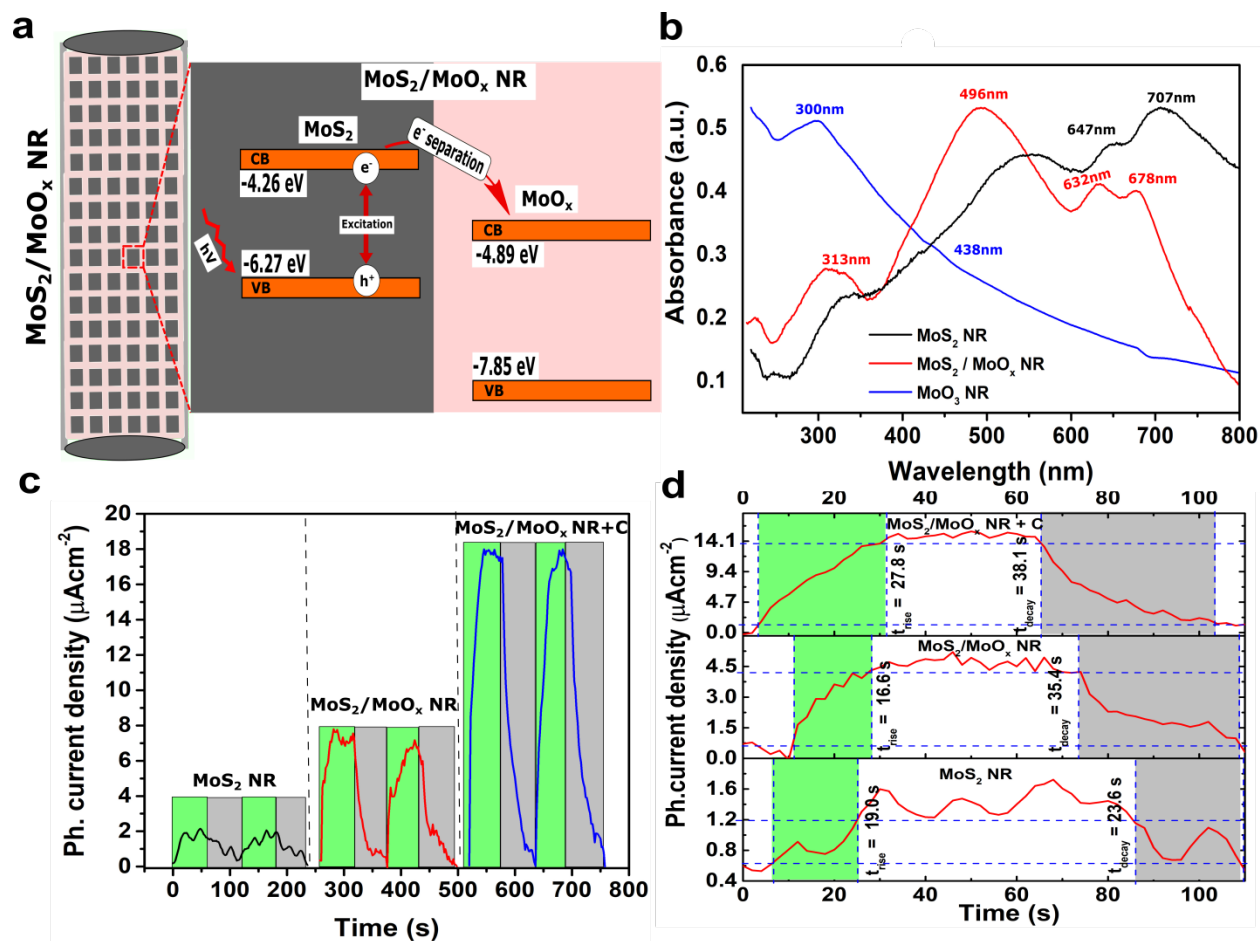


Figure 2. Optical response and charge transfer mechanism: (a) schematic electron-hole separation in the heterostructure $\text{MoS}_2/\text{MoO}_x$ NR (black- MoS_2 , light pink- MoO_x). (b) The UV-Vis spectra of MoO_3 (blue curve), heterostructure $\text{MoS}_2/\text{MoO}_x$ NR (red curve), and MoS_2 NR (black curve). (c) Comparison of the photoresponses of MoS_2 (black curve), $\text{MoS}_2/\text{MoO}_x$ NR, (red curve) and $\text{MoS}_2/\text{MoO}_x\text{NR}+\text{C}$ black (blue curve) at $V = 0.3$ V vs Ag/AgCl and power density 50 mW/cm 2 . (d) Comparison of photocurrent rise time and decay time of MoS_2 , $\text{MoS}_2/\text{MoO}_x$ NR and $\text{MoS}_2/\text{MoO}_x$ NR + C black.

As suggested by UV-Visible absorption spectra, there is no (negligible) absorption from MoO_3 NR in this frequency range since its absorption edge is at ~ 438 nm. The photoresponses of MoS_2 NR, $\text{MoS}_2/\text{MoO}_x$ NR, and $\text{MoS}_2/\text{MoO}_x$ NR + C black (the performance in the presence of

C- black is also tested because it is added with the active material during electrode fabrication for the battery) are measured, figure 2(c). The MoS₂/MoO_x NR + C showed the highest photocurrent density (~17 μA/cm²) followed by MoS₂/MoO_x (~8 μA/cm²), and MoS₂ (<2 μA/cm²). This significant photocurrent difference between MoS₂/MoO_x NR and MoS₂ NR clearly shows that the heterojunction of MoS₂/MoO_x NR helps in the charge separation of excitons formed during the light exposure because of the type II nature of the junction, as explained in figure 2 (a). The photoresponsivity is calculated with the formula $R_{\lambda} = \frac{I_{ph}}{PA}$, where R_{λ} is the photoresponsivity, I_{ph} is the photocurrent, P is the power density, and A is the effective area of the device. The photoresponsivity for MoS₂ NR, MoS₂/MoO_x NR, and MoS₂/MoO_x NR + C are calculated as 0.03, 0.15, and 0.32 mA/W, respectively. Low photoresponsivity of MoS₂ NR shows lack of photogenerated free charge carriers due to exciton formation. Figure 2(d) shows the measurement of response time of different systems. The response time for MoS₂ NR and MoS₂/MoO_x NR are ~ 19 s and ~16.8 s, respectively. Relatively faster response time in MoS₂/MoO_x NR compared to MoS₂ NR shows a clean interface between MoS₂ and MoO_x layers which is already evident from the STEM analyses. The MoS₂/MoO_x NR + C has a response time of ~ 27.8 s. This enhanced response time may be a result of the extra heterogenous interface of MoS₂ / MoO_x NR and carbon black. The interface is not atomically smooth and thus results in delayed response time. In addition to this, long-term photo response was also checked for MoS₂/MoO_x NRs in the presence of green and red light (figure S5). In both the cases, MoS₂/MoO_x NR shows high photoresponse as excitation frequency for MoS₂ matches in both the wavelengths.

c. Photo-Rechargeable Battery Construction and Performance:

As mentioned before, the heterostructures of 2D materials show high energy capacity in Li^+ storage compared with their individual 2D counterparts.²⁰ Herein, the conventional Li^+ battery performance of $\text{MoS}_2/\text{MoO}_x$ NR was initially tested and compared with that of MoO_x NR and MoS_2 NR (figure S6 (a-c)). It is observed that the specific capacity obtained for $\text{MoS}_2/\text{MoO}_x$ NR (600 mAh g^{-1} for the second cycle) is always higher than that of MoO_x NR (250 mAh g^{-1} for the second cycle) and MoS_2 NR (450 mAh g^{-1} for the second cycle). This ensures a better charge storage capacity of the as prepared $\text{MoS}_2/\text{MoO}_x$ NR heterostructure when compared to MoO_x NR or MoS_2 NR alone in a conventional Li battery coin cell (figure S6 (d)).

The photo-rechargeability of the $\text{MoS}_2/\text{MoO}_x$ NR in Li^+ battery was tested using a homebuilt photo-rechargeable battery (cell) setup (schematic and setup design are discussed in SI section-5 and figure S7). A light entering window is placed on the positive side while a lithium metal is placed at the negative side. To check the light assisted de-lithiation (or photo-charging) process of the $\text{MoS}_2/\text{MoO}_x$ NR electrode, the lithium half-cell was constructed showing the initial open circuit voltage (OCV) of 3.1 V. The cell was discharged in dark with 12 mA g^{-1} discharge current density (figure 3 (a), dark area). After a complete discharge (till it reaches ~ 0.01 V), the cell voltage was allowed to equilibrate (figure 3 (a), brown area) after the discharging.³⁹ After the voltage stabilization (at ~ 2.42 V), a red LED light having a power density of 50 mWcm^{-2} is turned on. The voltage enhancement is visible during the exposure of light as shown in figure 3 (a) (red area, enhanced up to 2.83 V within 4.7 h, *in situ* photo-

charging with light is shown in the supporting information video). This rise in the voltage is due to the light assisted de-lithiation or photo-charging of MoS₂/MoO_x NR electrode. To further confirm the effect of photo-charging on Li insertion and de-insertion in MoS₂/MoO_x NR electrode, cyclic voltammetry (CV) experiment was performed with Li-ion half-cells of MoS₂/MoO_x NR electrode with and without the exposure of light. The cyclic voltammogram (CV) was recorded in the range of 0.1-3.35V vs Li/Li⁺ at a scan rate of 1 mV/s (figure 3(b)). In the cathodic region, the peaks at 2.3 V and 1.85 V are attributed to Li⁺ insertion in MoO₃ and MoS₂, respectively.⁴⁰ Besides this, the peak at 0.6 V is related to the decomposition of the discharged species (Li_xMoO₃ and Li_xMoS₂) and formation of the solid electrolyte interphase (SEI). Further in the anodic region, the broad peak in the range of 1.4-2.2 V is related to the de-lithiation of Li_xMoS₂, oxidation of Mo to MoS₂ and MoO₃, and oxidation of Li₂S to sulphur and polysulfides.⁴⁰ All these characteristic peaks were observed in the presence of light as well. On the light exposure, the relative enhancements in the current density for all the redox peaks were observed. This can be attributed to the photo-current generated in the MoS₂/MoO_x NR electrode in the presence of light.

To confirm the light assisted de-lithiation in a lithiated MoS₂/MoO_x NR electrode, Raman spectra of the electrodes before and after light assisted de-lithiation were compared. Due to the lithiation in the MoS₂ of MoS₂/MoO_x NR, the phase transition of 2H phase to the 1T phase (figure 3 (c)) was happened. Further, the disappearance of B_{2g} mode of MoO_x NR is also observed because structure becomes highly disordered.¹⁵ A slight shift in the E_g and A_{1g} Raman modes can also be seen.⁴¹ On de-lithiation due to the photo-charging process, the 1T phase is found to be disappeared and so as the shift in E_g and A_{1g} modes of vibration (figure 3 (c)). As the holes are generated only in MoS₂, de-lithiation doesn't seem to be happened in the MoO_x and

hence the B_{2g} Raman modes of MoO_x is not restored after de-lithiation. But this issue can be addressed by electrochemical charging of the cell in definite intervals, as shown in the supporting information.

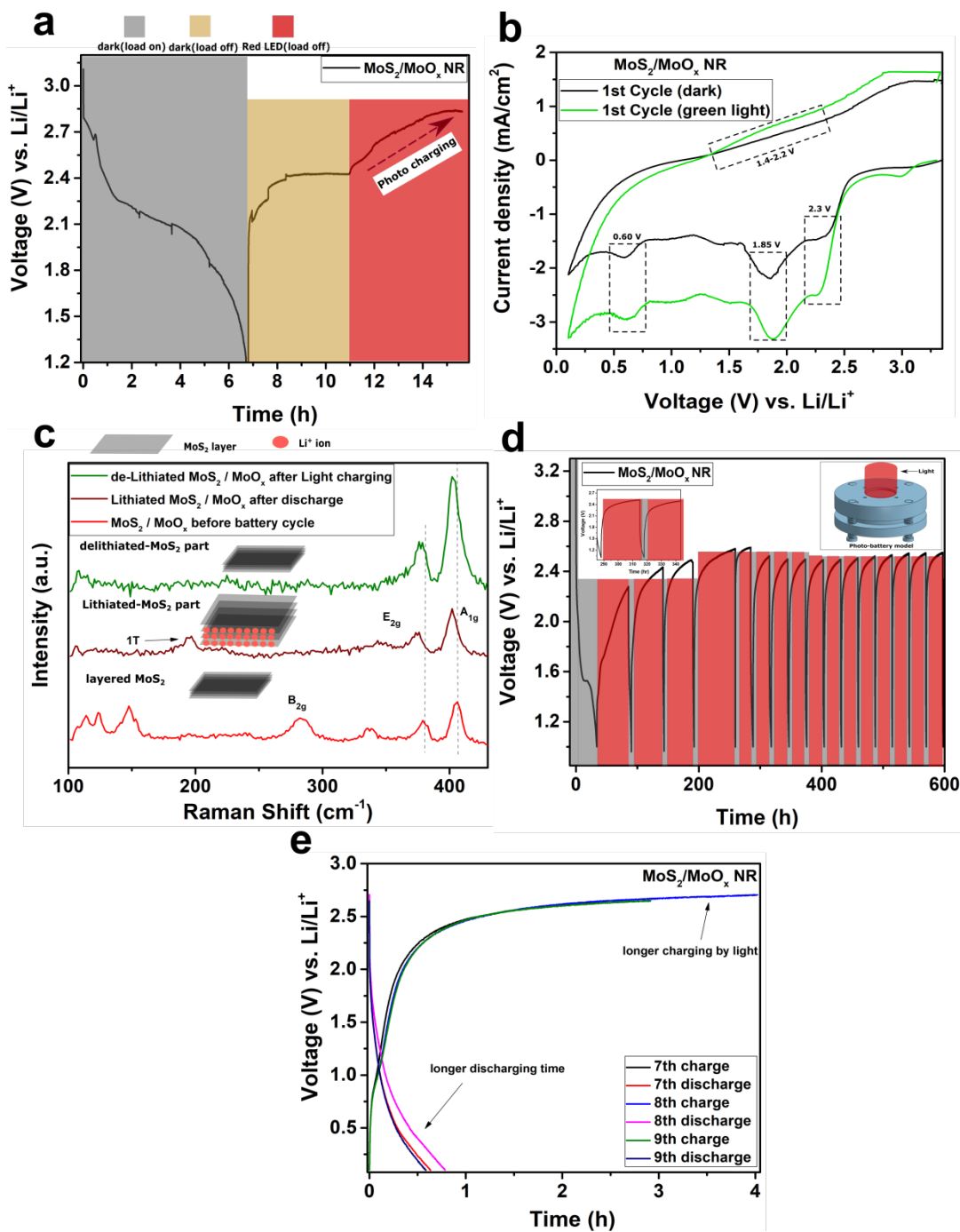


Figure 3. Photo charging and phase change traces by Raman spectroscopy: (a) Discharging in dark by constant current load (black area) followed by voltage equilibration (yellow area) and photo charging (red area). (b) Comparison of cyclic voltammogram (CV) of MoS₂/MoO_x NR electrodes (with Lithium metal as counter electrode) in dark and light at a scan rate of 1mV/s. (c) Comparison of the phase changes in MoS₂ (2H-1T-2H) before lithiation (red curve), after lithiation (brown curve), and after light-assisted de-lithiation (green curve) by Raman spectroscopy. (d) Long-term photo-battery cycling done at constant current for discharge and photo-assisted charge. (e) Comparison of the discharge time by varying photo-charging duration.

The long-term cyclability of this photo-rechargeable cell system is shown in figure 3 (d) (photographs of the setup in SI, figure S8). The discharge capacity is decreased from 120 mAhg⁻¹ for first light assisted discharge to 40 mAhg⁻¹ for 10th discharge. This charge storage capacity loss within few cycles is due to the fact that lithiation in MoO_x is not recovered during photo-charging because the hole generation happens in MoS₂ only, but can be recovered by electrochemical charging in definite intervals (as discussed before). Furthermore, during this long cycling, the discharge time always varies directly with charge time in the presence of light (figure 3 (e)). This confirms that the total charge capacity, hence the discharge capacity, depends on the duration of light exposure (number of photons absorbed) in the photo assisted de-lithiation process in the MoS₂/MoO_x NR electrode.

The discharge of the cell is also checked in the presence of light and compared with that in the dark. Due to the competitive charging process, the discharge capacity is found to be increased from 69 mAh g⁻¹ in dark to 162 mAh g⁻¹ in the presence of light (figure 4 (a)). This

enhancement in the energy efficiency in the presence of light shows the performance of $\text{MoS}_2/\text{MoO}_x$ NR electrode based photoelectrodes (figure 4 (b), details in SI, section-6).

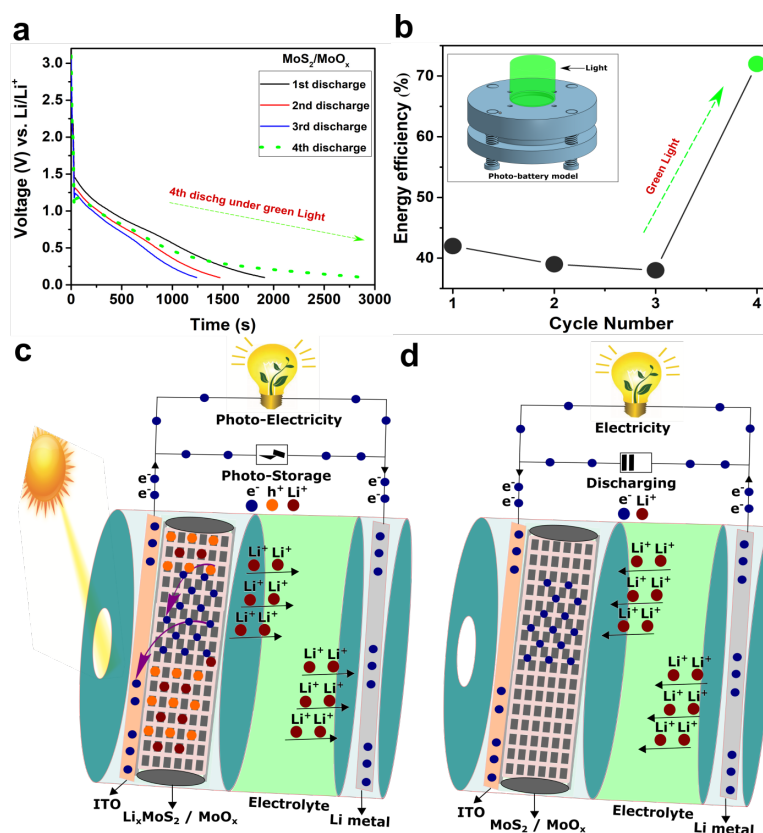


Figure 4. (a) Competitive photo-charging during the discharge of the battery with $\text{MoS}_2/\text{MoO}_x$ photo-electrode. (b) Energy efficiency (%) for discharge in dark at constant current load for three cycles and discharge in green LED during the fourth cycle (inset photo-battery model with a light window). (c) Schematic illustrations of simultaneous photo-storage and photo-electricity

generation by a single nanostructured type II semiconductor heterostructure of MoS₂/MoO_x NR with Li metal as the counter electrode in a two-electrode photo-rechargeable battery. (d) Schematic showing the use of stored electrochemical energy in the absence of light.

Finally, the mechanism of photo-charging on the MoS₂/MoO_x NR based photoelectrode for Li⁺ cell is proposed here. Semiconductor I (MoS₂) acts as both lithium storage and light absorbing material where photoelectrons are generated on light exposure. While, semiconductor II (MoO_x) acts as a separator electrode of electron-hole pairs generated in MoS₂. When light falls on a lithiated MoS₂/MoO_x NR *via* transparent ITO coated glass electrode (figure 4 (c)), the holes accumulated in MoS₂ pushes Li⁺ ions towards the anode where they get neutralized by photoelectrons. As in a conventional Li ion battery, Li metal spontaneously oxidize to Li⁺ ions during discharging and the generated Li⁺ ions get intercalated in the MoS₂/MoO_x NR (figure 4 (d)).

In conclusion, a two-electrode photo-rechargeable Li⁺ battery (single cell) is demonstrated here. A type-II semiconductor heterostructure having staggered optical band gap alignment formed due to the in-plane bonding of MoS₂ and MoO_x is used as a photo-electrode for battery recharging. After establishing the structure, photoelectron generation, and charge separation in this heterostructure (MoS₂/MoO_x), construction of a solar battery of MoS₂/MoO_x with Li metal as the other electrode shows the potential of such semiconductors-based stable (>15 cycles are shown here) electrodes in photo-recharging, contrary to other unstable electrodes in the present literature. In this cell, the discharge capacity is found to be increased from 69 mAh g⁻¹ in dark to 162 mAh g⁻¹ in the presence of light, indicating the enhancement in the energy efficiency to ~ 70% in light (green, 50 mW). This opens up the potential in developing

semiconductor heterostructures based novel photo-electrode designs in solar batteries, where they can ensure high light-matter interaction with small exciton binding energy in comparison to that in organic materials, high electrolyte stability, large metal ion intercalation area, and hence high energy efficient, high-capacity solar batteries.

Acknowledgements:

Authors thank the support of the Department of Atomic Energy, Government of India, under Project Identification No. RTI 4007. Authors thank Dr. Pranav R. Shirhatti for his valuable suggestions on designing and understanding the photo-battery model.

Supporting Information:

The details of the coin cell performance, materials synthesis, photo-rechargeable cell design, STEM-HAADF images, SEM images, EDS mapping etc. are available in the supporting information.

References

1. Vega-Garita, V.; Hanif, A.; Narayan, N.; Ramirez-Elizondo, L.; Bauer, P., Selecting a suitable battery technology for the photovoltaic battery integrated module. *Journal of Power Sources* **2019**, *438*, 227011.
2. Xu, J.; Chen, Y.; Dai, L., Efficiently photo-charging lithium-ion battery by perovskite solar cell. *Nat Commun* **2015**, *6* (1), 1-7.
3. Li, Q.; Liu, Y.; Guo, S.; Zhou, H., Solar energy storage in the rechargeable batteries. *Nano Today* **2017**, *16*, 46-60.
4. Rizzo, G., Automotive applications of solar energy. *IFAC Proceedings Volumes* **2010**, *43* (7), 174-185.
5. Klesh, A. T.; Kabamba, P. T., Solar-powered aircraft: Energy-optimal path planning and perpetual endurance. *Journal of guidance, control, and dynamics* **2009**, *32* (4), 1320-1329.
6. Vertat, I.; Vobornik, A., Efficient and reliable solar panels for small CubeSat picosatellites. *International Journal of Photoenergy* **2014**, *2014*.
7. Hodes, G.; Manassen, J.; Cahen, D., Photoelectrochemical energy conversion and storage using polycrystalline chalcogenide electrodes. *Nature* **1976**, *261* (5559), 403-404.
8. Monassen, J.; Hodes, G.; Cahen, D., Photoelectrochemical Energy Conversion and Storage: The Polycrystalline Cell with Different Storage Modes. *J Electrochem Soc* **1977**, *124* (4), 532.
9. Paoletta, A.; Faure, C.; Bertoni, G.; Marras, S.; Guerfi, A.; Darwiche, A.; Hovington, P.; Commariou, B.; Wang, Z.; Prato, M., Light-assisted delithiation of lithium iron phosphate nanocrystals towards photo-rechargeable lithium ion batteries. *Nat Commun* **2017**, *8* (1), 1-10.
10. Ahmad, S.; George, C.; Beesley, D. J.; Baumberg, J. J.; De Volder, M., Photo-rechargeable organo-halide perovskite batteries. *Nano letters* **2018**, *18* (3), 1856-1862.
11. Kato, K.; Puthirath, A. B.; Mojibpour, A.; Miroshnikov, M.; Satapathy, S.; Thangavel, N. K.; Mahankali, K.; Dong, L.; Arava, L. M. R.; John, G., Light-Assisted Rechargeable Lithium Batteries: Organic Molecules for Simultaneous Energy Harvesting and Storage. *Nano letters* **2021**, *21* (2), 907-913.
12. Hu, Z.; Liu, Q.; Chou, S.-L.; Dou, S.-X., Two-dimensional material-based heterostructures for rechargeable batteries. *Cell Reports Physical Science* **2021**, 100286.
13. Rasmussen, F. A.; Thygesen, K. S., Computational 2D materials database: electronic structure of transition-metal dichalcogenides and oxides. *The Journal of Physical Chemistry C* **2015**, *119* (23), 13169-13183.
14. Suslov, E. A.; Bushkova, O. V.; Sherstobitova, E. A.; Reznitskikh, O. G.; Titov, A. N., Lithium intercalation into TiS₂ cathode material: phase equilibria in a Li–TiS₂ system. *Ionics* **2016**, *22* (4), 503-514.
15. Lee, S. H.; Kim, Y. H.; Deshpande, R.; Parilla, P. A.; Whitney, E.; Gillaspie, D. T.; Jones, K. M.; Mahan, A. H.; Zhang, S.; Dillon, A. C., Reversible lithium-ion insertion in molybdenum oxide nanoparticles. *Advanced Materials* **2008**, *20* (19), 3627-3632.
16. Kim, H.-S.; Cook, J. B.; Lin, H.; Ko, J. S.; Tolbert, S. H.; Ozolins, V.; Dunn, B., Oxygen vacancies enhance pseudocapacitive charge storage properties of MoO_{3-x}. *Nat Mater* **2017**, *16* (4), 454-460.
17. Stephenson, T.; Li, Z.; Olsen, B.; Mitlin, D., Lithium ion battery applications of molybdenum disulfide (MoS₂) nanocomposites. *Energ Environ Sci* **2014**, *7* (1), 209-231.

18. Park, J.; Kim, J.-S.; Park, J.-W.; Nam, T.-H.; Kim, K.-W.; Ahn, J.-H.; Wang, G.; Ahn, H.-J., Discharge mechanism of MoS₂ for sodium ion battery: Electrochemical measurements and characterization. *Electrochimica Acta* **2013**, *92*, 427-432.
19. Ren, X.; Zhao, Q.; McCulloch, W. D.; Wu, Y., MoS₂ as a long-life host material for potassium ion intercalation. *Nano Research* **2017**, *10* (4), 1313-1321.
20. Pomerantseva, E.; Gogotsi, Y., Two-dimensional heterostructures for energy storage. *Nature Energy* **2017**, *2* (7), 1-6.
21. San Martín, S.; Rivero, M. J.; Ortiz, I., Unravelling the Mechanisms that Drive the Performance of Photocatalytic Hydrogen Production. *Catalysts* **2020**, *10* (8), 901.
22. Wang, J.; Zhao, J.; Osterloh, F., Photochemical charge transfer observed in nanoscale hydrogen evolving photocatalysts using surface photovoltage spectroscopy. *Energ Environ Sci* **2015**, *8* (10), 2970-2976.
23. Mahmood, N.; Hou, Y., Electrode nanostructures in lithium-based batteries. *Advanced Science* **2014**, *1* (1), 1400012.
24. Li, H.; Yu, K.; Tang, Z.; Fu, H.; Zhu, Z., High photocatalytic performance of a type-II α -MoO₃@ MoS₂ heterojunction: From theory to experiment. *Phys Chem Chem Phys* **2016**, *18* (20), 14074-14085.
25. Patel, S. K. S.; Dewangan, K.; Srivastav, S. K.; Verma, N. K.; Jena, P.; Singh, A. K.; Gajbhiye, N., Synthesis of α -MoO₃ nanofibers for enhanced field-emission properties. *Adv. Mater. Lett.* **2018**, *9* (8), 585.
26. Li, B.; Jiang, L.; Li, X.; Ran, P.; Zuo, P.; Wang, A.; Qu, L.; Zhao, Y.; Cheng, Z.; Lu, Y., Preparation of monolayer MoS₂ quantum dots using temporally shaped femtosecond laser ablation of bulk MoS₂ targets in water. *Sci Rep-Uk* **2017**, *7* (1), 1-12.
27. Golovynskiy, S.; Irfan, I.; Bosi, M.; Seravalli, L.; Datsenko, O. I.; Golovynska, I.; Li, B.; Lin, D.; Qu, J., Exciton and trion in few-layer MoS₂: thickness- and temperature-dependent photoluminescence. *Applied Surface Science* **2020**, *515*, 146033.
28. Dieterle, M.; Weinberg, G.; Mestl, G., Raman spectroscopy of molybdenum oxides Part I. Structural characterization of oxygen defects in MoO_{3-x} by DR UV/VIS, Raman spectroscopy and X-ray diffraction. *Phys Chem Chem Phys* **2002**, *4* (5), 812-821.
29. Chen, Z.; Cummins, D.; Reinecke, B. N.; Clark, E.; Sunkara, M. K.; Jaramillo, T. F., Core-shell MoO₃-MoS₂ nanowires for hydrogen evolution: a functional design for electrocatalytic materials. *Nano letters* **2011**, *11* (10), 4168-4175.
30. Zhang, C.; Wang, Z.; Bhoyate, S.; Morey, T.; Neria, B. L.; Vasiraju, V.; Gupta, G.; Palchoudhury, S.; Kahol, P.; Mishra, S., MoS₂ decorated carbon nanofibers as efficient and durable electrocatalyst for hydrogen evolution reaction. *c* **2017**, *3* (4), 33.
31. Muijsers, J.; Weber, T.; Vanhardeveld, R.; Zandbergen, H.; Niemantsverdriet, J., Sulfidation study of molybdenum oxide using MoO₃/SiO₂/Si (100) model catalysts and Mo-IV₃-sulfur cluster compounds. *Journal of Catalysis* **1995**, *157* (2), 698-705.
32. Wongkrua, P.; Thongtem, T.; Thongtem, S., Synthesis of h- and α -MoO₃ by refluxing and calcination combination: Phase and morphology transformation, photocatalysis, and photosensitization. *Journal of Nanomaterials* **2013**, *2013*.
33. Visic, B.; Dominko, R.; Gunde, M. K.; Hauptman, N.; Skapin, S. D.; Remskar, M., Optical properties of exfoliated MoS₂ coaxial nanotubes-analogues of graphene. *Nanoscale research letters* **2011**, *6* (1), 1-6.

34. Jeon, J.; Jang, S. K.; Jeon, S. M.; Yoo, G.; Jang, Y. H.; Park, J.-H.; Lee, S., Layer-controlled CVD growth of large-area two-dimensional MoS₂ films. *Nanoscale* **2015**, *7* (5), 1688-1695.
35. Bai, H.; Yi, W.; Li, J.; Xi, G.; Li, Y.; Yang, H.; Liu, J., Direct growth of defect-rich MoO_{3-x} ultrathin nanobelts for efficiently catalyzed conversion of isopropyl alcohol to propylene under visible light. *J Mater Chem A* **2016**, *4* (5), 1566-1571.
36. Krishna, A. G.; Ravikumar, R.; Kumar, T. V.; Ephraim, S. D.; Ranjith, B.; Pranoy, M.; Dola, S., Investigation and comparison of optical and raman bands of mechanically synthesised MoO₃ nano powders. *Materials Today: Proceedings* **2016**, *3* (1), 54-63.
37. Kaushik, V.; Wu, S.; Jang, H.; Kang, J.; Kim, K.; Suk, J. W., Scalable exfoliation of bulk MoS₂ to single-and few-layers using toroidal taylor vortices. *Nanomaterials* **2018**, *8* (8), 587.
38. SAKHONWASEE, S.; TUMMACHAI, K.; NIMNOY, N., Influences of LED light quality and intensity on stomatal behavior of three petunia cultivars grown in a semi-closed system. *Environmental Control in Biology* **2017**, *55* (2), 93-103.
39. Hu, Y.; Iwata, G. Z.; Mohammadi, M.; Silletta, E. V.; Wickenbrock, A.; Blanchard, J. W.; Budker, D.; Jerschow, A., Sensitive magnetometry reveals inhomogeneities in charge storage and weak transient internal currents in Li-ion cells. *Proceedings of the National Academy of Sciences* **2020**, *117* (20), 10667-10672.
40. Zhao, S.; Zha, Z.; Liu, X.; Tian, H.; Wu, Z.; Li, W.; Sun, L.-B.; Liu, B.; Chen, Z., Core-Sheath Structured MoO₃@ MoS₂ Composite for High-Performance Lithium-Ion Battery Anodes. *Energy & Fuels* **2020**, *34* (9), 11498-11507.
41. Xia, J.; Wang, J.; Chao, D.; Chen, Z.; Liu, Z.; Kuo, J.-L.; Yan, J.; Shen, Z. X., Phase evolution of lithium intercalation dynamics in 2H-MoS₂. *Nanoscale* **2017**, *9* (22), 7533-7540.

Supplementary Materials

Photo Rechargeable Li-Ion Batteries using Nanorod Heterostructure

Electrodes

Amar Kumar^a, Pallavi Thakur^a, Rahul Sharma^a, Anand Puthirath^b, Pulickel M. Ajayan^b, and

Tharangattu N. Narayanan^{a*}

^a Tata Institute of Fundamental Research - Hyderabad, Hyderabad, Telangana 500046, India

^b Department of Materials Science and Nano-engineering, Rice University, Houston, Texas
77005, United States

(Email*: tnn@tifrh.res.in)

This file includes:

Section 1: Experimental section

- Materials & Methods
- Preparation of Electrodes
- Characterization

Section 2: SEM, Raman spectroscopy, XPS, HAADF analysis and photoresponse MoO₃, MoS₂ and MoS₂/MoO_x NRs

- Figure S1: SEM and EDS mapping of MoO₃, MoS₂/MoO_x and MoS₂ NR
- Figure S2: Raman spectroscopy analysis for MoS₂/MoO_x NR
- Figure S3: High resolution XPS spectra for MoO₃, MoS₂/MoO_x and MoS₂ NR
- Figure S4: HAADF-STEM images and elemental mapping of MoS₂/MoO_x NR and MoS₂ NR

Section 3: Band structure of MoO₃, MoS₂ and MoS₂ / MoO_x

- Figure S5: Photo-response of MoS₂/MoO_xNR in Red and Green LED

Section 4: Conventional Li-ion battery performance of MoS₂ / MoO_x NR

- Figure S6: Conventional Li⁺-ion battery performance of MoO₃, MoS₂/MoO_x and MoS₂ NR

Section 5: Photo-rechargeable battery model and assembly process

- Figure S7: Schematic of photo-rechargeable model
- Figure S8: Photograph of working photo-rechargeable battery

Section 6: Energy efficiency calculation

Section 1: Experimental section

- **Materials & Methods:**

Materials: -

Ammonium molybdatetetrahydrate (SRL), Nitric acid (Sigma-Aldrich), Sulphur (SigmaAldrich), Lithium hexa fluoro phosphate in EC/EMC solvent (SigmaAldrich), ITO coated glass 25mm x 25 mm (Sigma-Aldrich)

Methods:

Chemical Synthesis: Firstly, MoO₃ NR are synthesised by hydrothermal process.¹ For that 1.0 g Ammonium molybdatetetrahydrate was dissolved in 80 ml deionized water. Then, 6 ml of 65% nitric acid was slowly added in the above solution. After 30 minutes of magnetic stirring, the above solution was transferred in a 100 ml Teflon autoclave and heated at 180 °C for 12 h. After this, the solution is kept to cool down in room temperature. The obtained white compound was washed by deionised water and ethanol for many times and then dried at 60 °C in dry oven.

The growth MoO₃ is α type, Mechanism involve in this can be formulated as in equation 1 to 3.



Further, to synthesize MoS₂/MoO_x NR heterostructure, MoS₂ growth was done on MoO₃ by CVD in two zone furnaces. For deposition, a glass tube with sulphur powder as a sulphur source is heated in the first zone at 230°C while MoO₃ NR is kept in the second zone at 450°C with 20 minutes ramping and 5-minute growth time. To maintain the inert environment, a continuous flow of N₂ gas at 85 SCCM is allowed to pass. Further, for comparison MoS₂ NR were also synthesized with growth time of 20 minutes in the same environment.

- **Preparation of Electrodes:**

For electrode fabrication, the sample was mixed with 10% carbon black and 10 % PVDF binder. Mixed well in NMP solvent and dropcasted on ITO coated glass. The coating was further dried at 80° C for 4 hr.

- **Characterisation:**

To determine vibrational modes of MoS₂ and MoO₃, Renishaw in Via Raman Microscope (532 nm excitation) was used. Further to know the surface topography and composition of the sample, scanning electron microscopy ((SEM)(FESEM) JEOL JSM-7200F) along with Energy Dispersive X-Ray Spectroscopy (EDS or EDX) was used. To identify elemental composition in material or on surface and chemical state we used PHI Quantera X-ray photoelectron spectrometer (Survey: pass energy, 140 eV, high-resolution spectra, 26 eV). Casaxps software was used for curve fitting. The nano-scale and atomic-scale structure of material was checked by Titan transmission electron microscope (TEM) (FEI Titan Themis 3 with acceleration voltage of 300 kV). Crystallinity of material was checked by X-ray diffraction (Bruker Tensor-27). UV-VIS spectra (JASCO V-670) was recorded within 200 to 800 nm range. Photo activity was checked in three electrode system with Ag/AgCl reference and graphite as counter in Potentiostat, Biologic SP-300. For this, the sample was coated on glassy carbon and applied 0.3 V external bias in 0.1 M Na₂SO₄. Green and red LED light were used for regular on and off.

Section 2: SEM, Raman spectroscopy, XPS, HAADF analysis and photoresponse
MoO₃, MoS₂ and MoS₂ / MoO_x NRs:

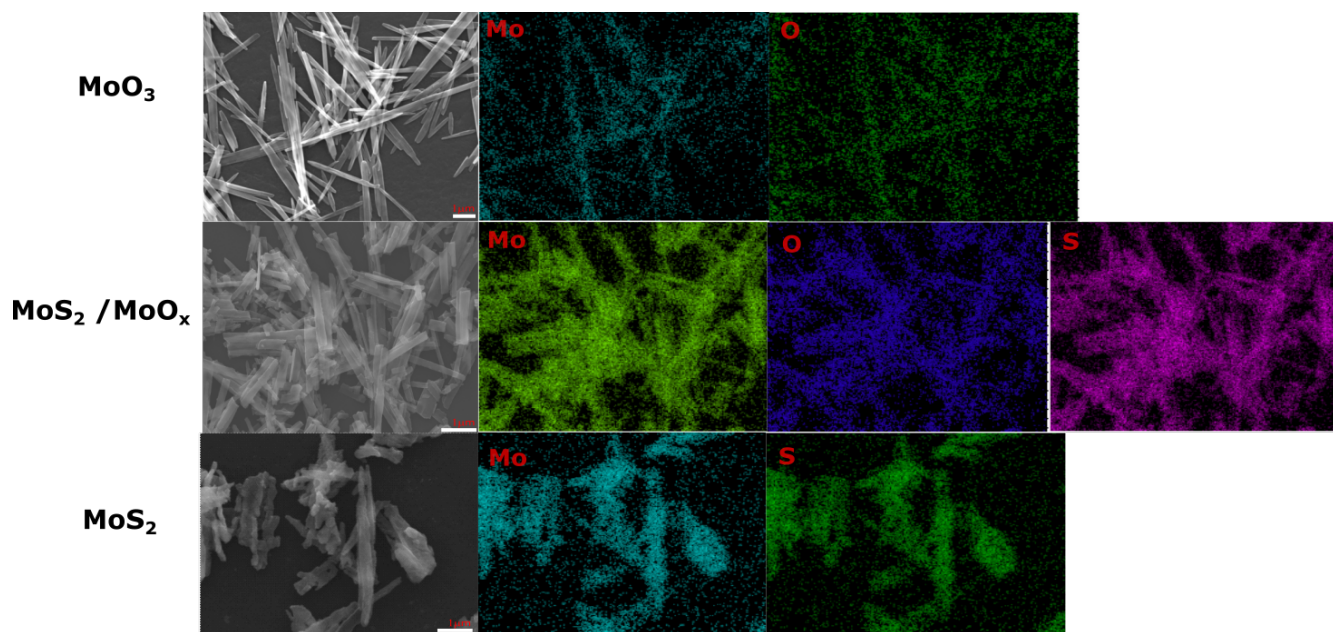


Figure S1. SEM and EDS mapping of MoO₃, MoS₂/MoO_x and MoS₂ NR

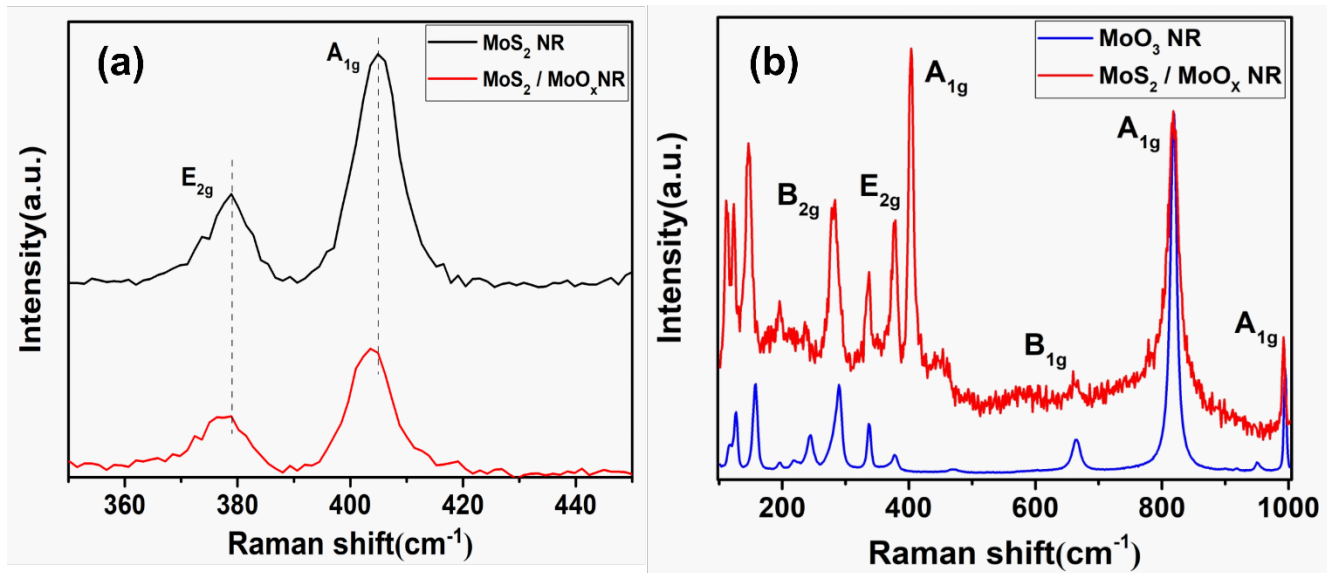


Figure S2. (a) Comparison of Raman shift of MoS₂ / MoO_x (red curve) and MoS₂NR (black curve) (b) Raman modes broadening comparison between of MoS₂ / MoO_x and MoO₃ NR

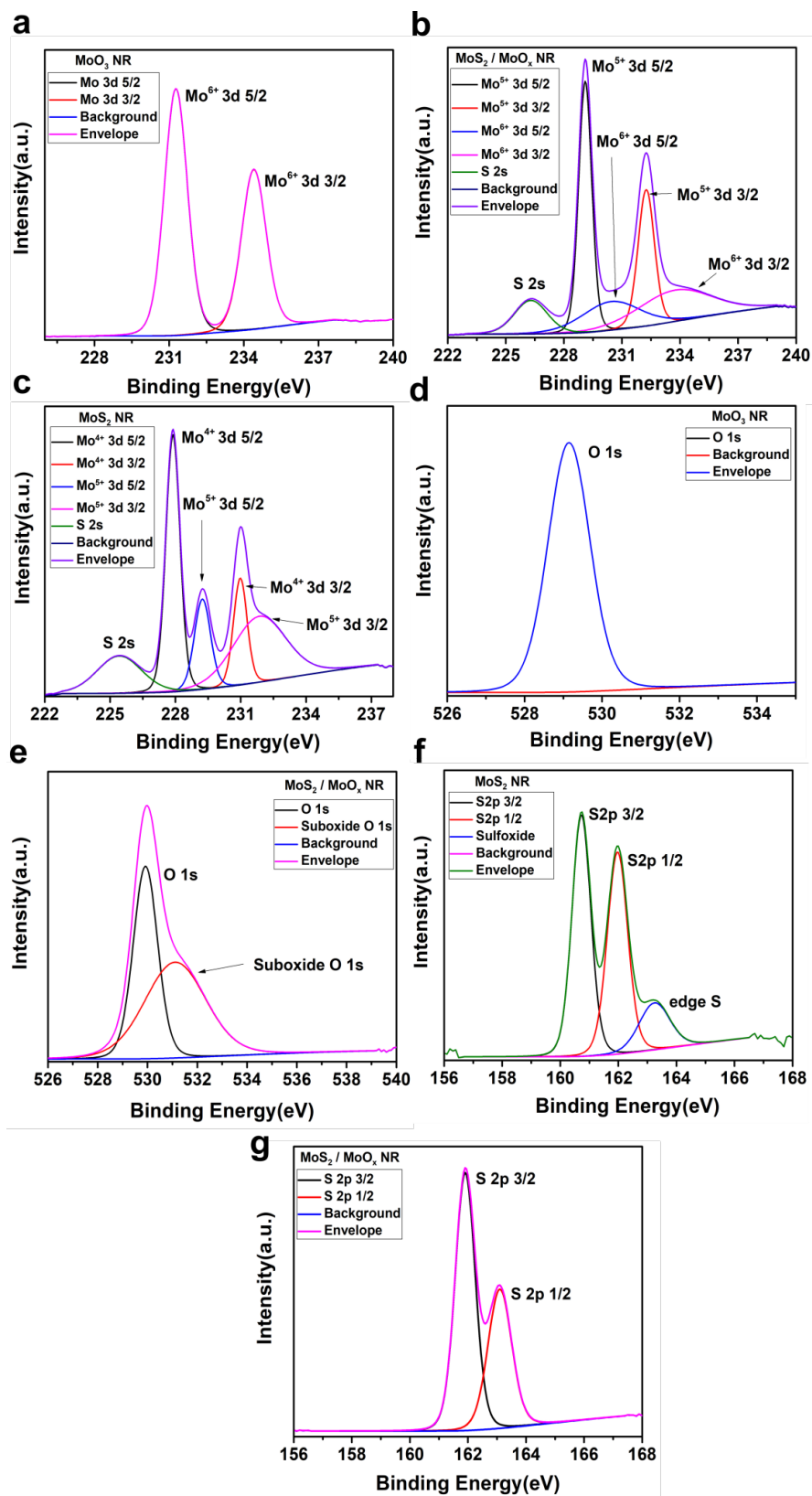


Figure S3:- High resolution XPS spectra of (a) Mo 3d of MoO₃NR (b) Mo 3d of MoS₂/MoO_xNR (c) Mo 3d of MoS₂NR (d) O 1s of MoO₃NR (e) O 1s of MoS₂/MoO_xNR (f) S 2p of MoS₂NR (g) S 2p of MoS₂/ MoO_xNR

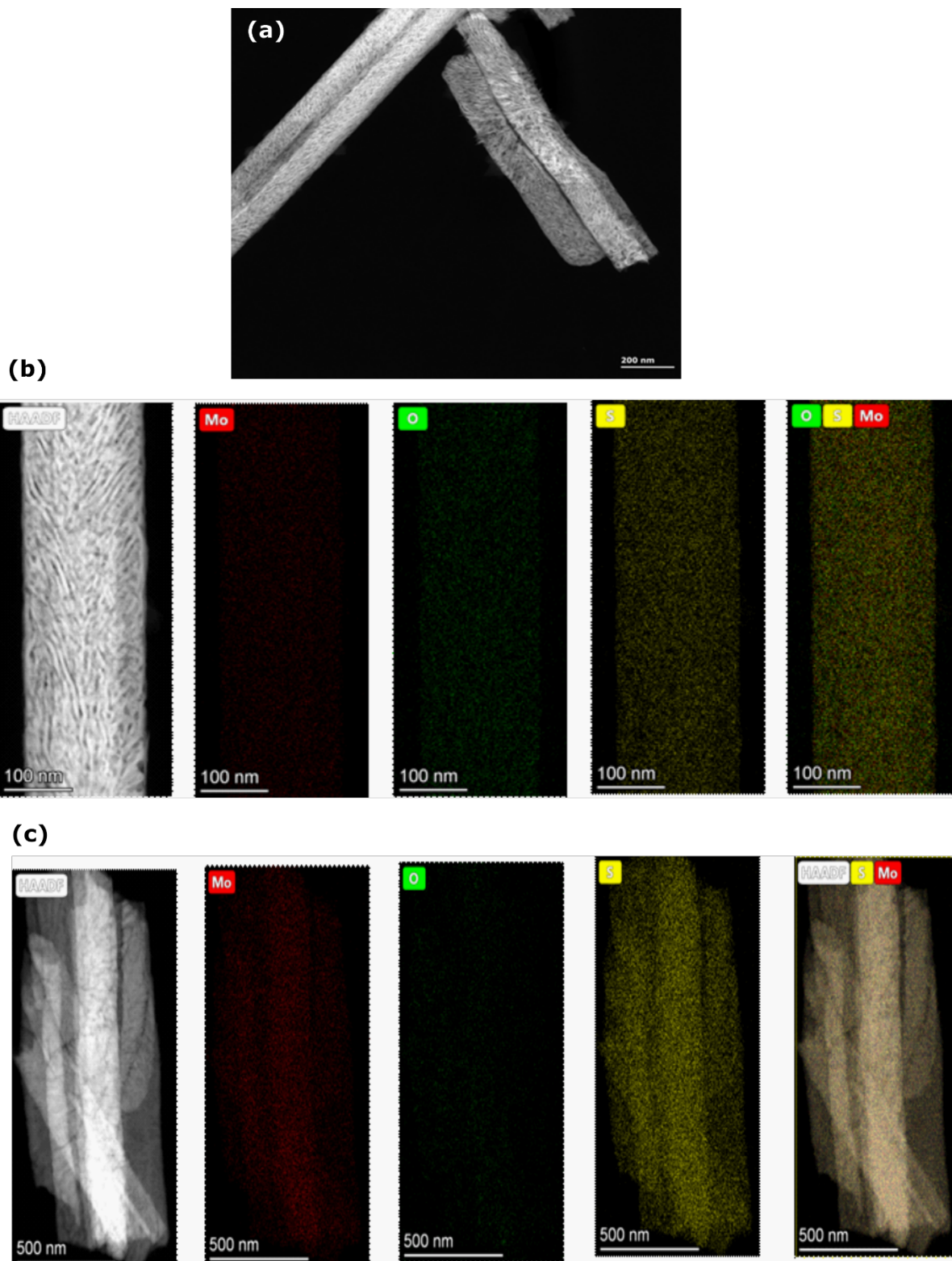


Figure S4. HAADF-STEM (a) image and elemental mapping (a-b) of MoS₂/MoO_xNR and MoS₂ NR

Section 3: Band structure of MoO_3 , MoS_2 and $\text{MoS}_2 / \text{MoO}_x$:

DFT calculations of MoO_3 shows that its band gap is 2.6 eV.² The Valence band (VB) of α - MoO_3 is mainly composed of O p states, while the Conduction band (CB) is formed mainly by Mo 4d states. This shows the band position at -9.66 eV (VB) and -6.96 eV (CB). However, this get changed when MoO_3 converts as MoO_x to -7.58 eV (VB) and -4.89 eV (CB).³ Further, MoS_2 VB mainly composed of S p states, while the Conduction band (CB) is formed mainly by Mo 4d states. This shows band position at -6.27 eV (VB) and -4.25 eV (CB).⁴ In $\text{MoS}_2/\text{MoO}_x$ both the semiconductors make perfect staggered Type II Hetero-structure as shown figure 2 (a). When the incident light energy matches with MoO_x band gap energy, the photons get absorbed. This excites the electrons from VB to CB. Similarly, electrons get excited in MoS_2 too. However, due to staggered band alignment, electrons flow from MoS_2 to MoO_x and hole transfer from MoO_3 to MoS_2 VB. This makes the charge separation easier in $\text{MoS}_2/\text{MoO}_x\text{NR}$.

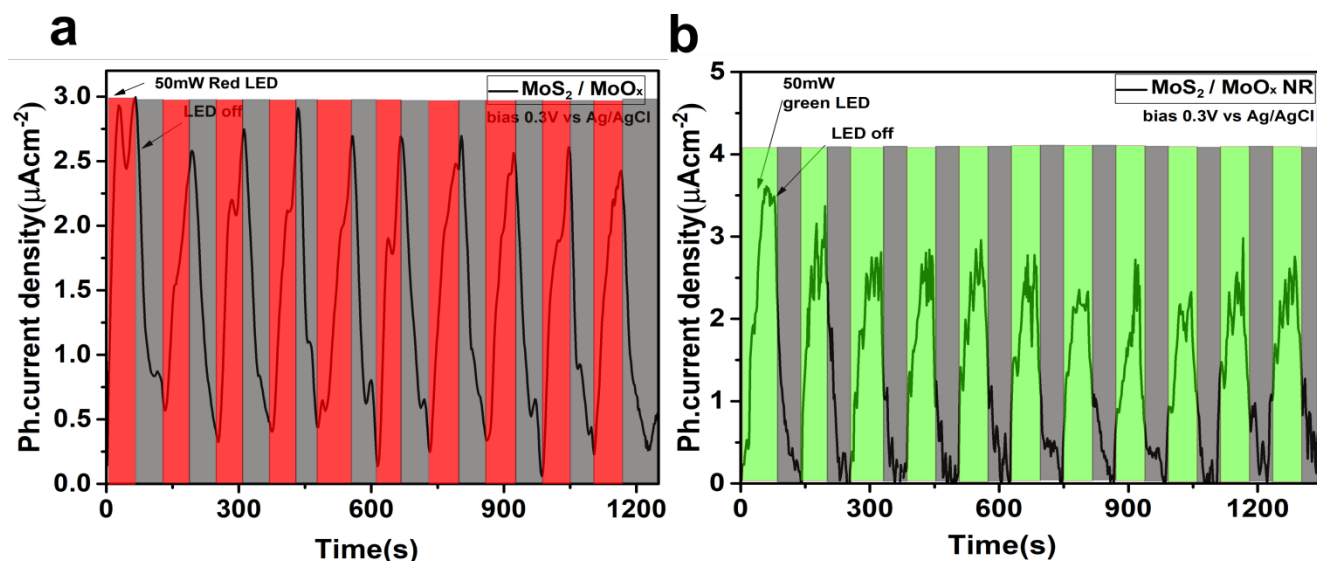


Figure S5. Photo-response of $\text{MoS}_2/\text{MoO}_x\text{NR}$ in (a) Red and (b) Green LED light

Section 4: Conventional Li-ion battery performance of $\text{MoS}_2 / \text{MoO}_x$ NR:

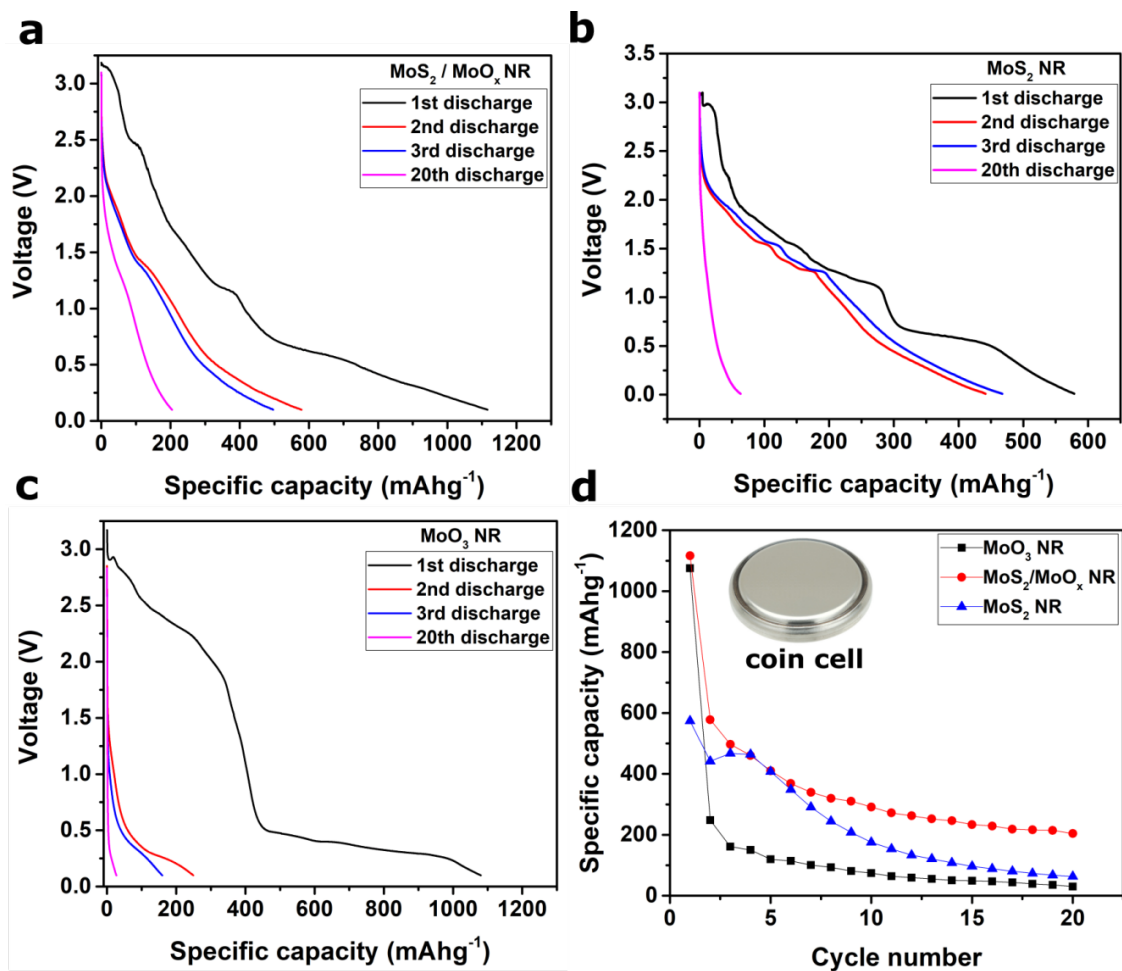


Figure S6. Conventional Li^+ ion battery performance of (a) $\text{MoS}_2 / \text{MoO}_x$ NR, (b) MoS_2 NR, (c) MoO_3 NR (d) comparison of specific capacity for all electrodes.

Section 5:Photo-rechargeable battery model and assembly process:

To perform experiments in ambient condition, a lab-made photo-rechargeable model with light window (figure S2) was used. The model positive case (I) is made of steel with 65 mm diameter and 16 mm thickness. A 4 mm thick O-ring with 20 mm diameter at 8.7 mm depth was placed in positive case (I) to make it completely air tight. A 17 mm diameter wide hole is made in positive case (I) as light window where 25*25 mm sample containing ITO coated glass (IV) is placed. Further, the conducting side of ITO is connected with positive case by copper foil (III), sealed by nut using 31 outer and 17 mm inner diameter aluminum ring (V). An O-ring was used in both side of ITO coated glass to seal air tight from bottom side and a Teflon separator (II) which separate positive and negative case. After that, separator (VI) lithium metal (VII), steel disc (VIII), one spring for better connectivity (IX), (45-35) mm diameter negative case (X) were assembled as shown in figure S1. box.

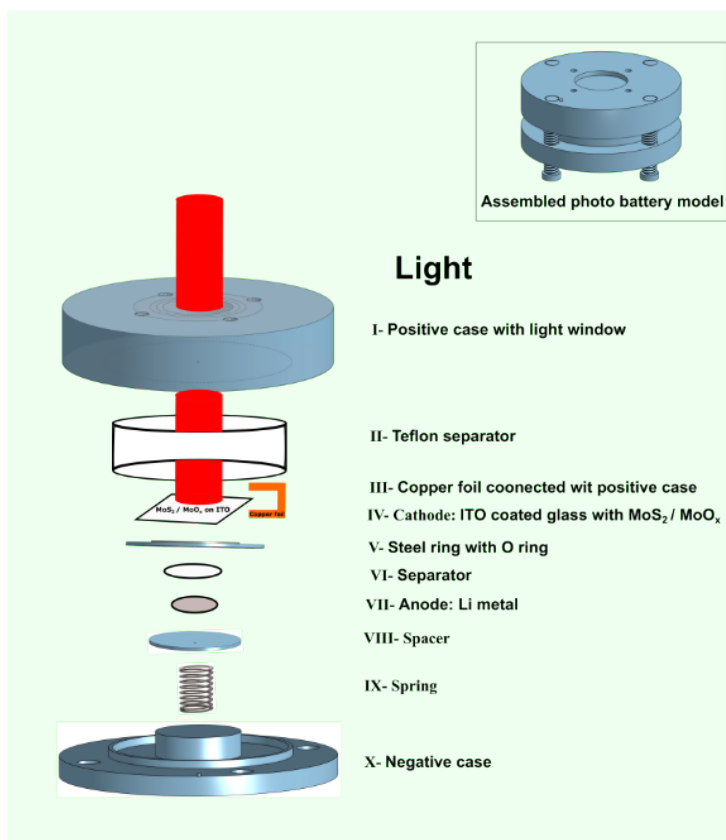


Figure S7. Schematic of photo-rechargeable home-built battery model and its assembly model in inset

The assembly was made in an Ar filled glove.

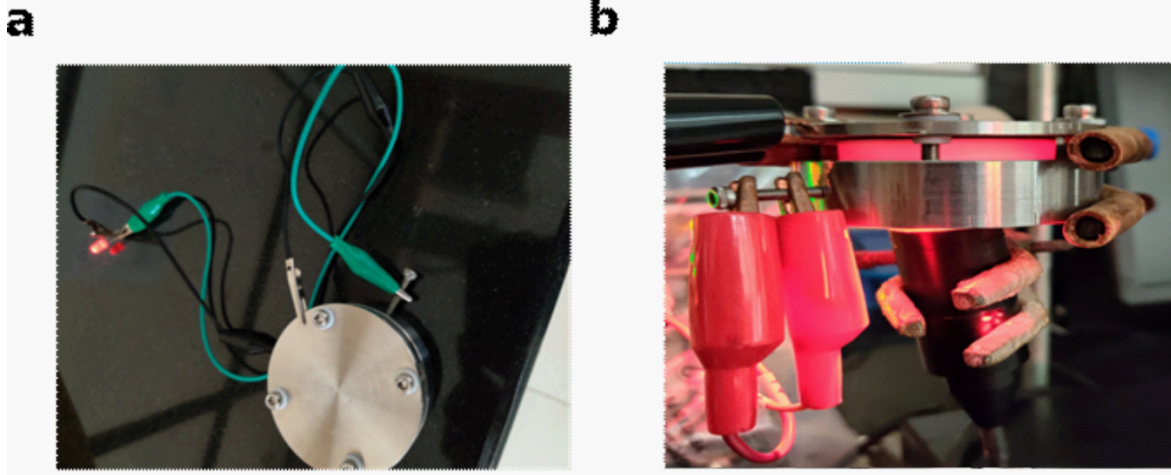


Figure S8. Figure S8. (a) Photograph of a working photo-chargeable cell on an LED load. (b) Photograph of the photo-charging of the cell by light.

Section 6: Energy efficiency:

Energy efficiency is calculated by taking ratio of discharge and charge profile curves. During charging and discharging, it is evident that the voltage supplied for charging is higher than the cell voltage during the battery usage, and obviously, the energy efficiency is poor⁵ that we can see in figure 4 (b).

References

1. Li, H.; Yu, K.; Tang, Z.; Fu, H.; Zhu, Z., High photocatalytic performance of a type-II α -MoO₃@ MoS₂ heterojunction: From theory to experiment. *Phys Chem Chem Phys* **2016**,*18* (20), 14074-14085.
2. Du, Y.; Peng, H. Y.; Mao, H.; Jin, K. X.; Wang, H.; Li, F.; Gao, X. Y.; Chen, W.; Wu, T., Evolution of the SrTiO₃-MoO₃ interface electronic structure: An in situ photoelectron spectroscopy study. *Acs Appl Mater Inter* **2015**,*7* (21), 11309-11314.
3. Butler, K. T.; Crespo-Otero, R.; Buckeridge, J.; Scanlon, D. O.; Bovill, E.; Lidzey, D.; Walsh, A., Band energy control of molybdenum oxide by surface hydration. *Applied Physics Letters* **2015**,*107* (23), 231605.
4. Lee, S.; Zhong, Z., Nanoelectronic circuits based on two-dimensional atomic layer crystals. *Nanoscale* **2014**,*6* (22), 13283-13300.
5. Eftekhari, A., Energy efficiency: a critically important but neglected factor in battery research. *Sustainable Energy & Fuels* **2017**,*1* (10), 2053-2060.